Searches for neutrino counterparts of gravitational waves from the LIGO/Virgo third observing run with KM3NeT

Journal of Cosmology and Astroparticle Physics
An IOP and SISSA journal

Received: November 8, 2023
Revised: January 30, 2024
Accepted: February 27, 2024
Published: April 9, 2024

Searches for neutrino counterparts of gravitational waves from the LIGO/Virgo third observing run with KM3NeT

The KM3NeT collaboration

S. Aiello,[a] A. Albert,[b,bc] S. Alves Garre,[c] Z. Aly,[d] A. Ambrosone,[f,e] F. Ameli,[g] M. Andre,[h] E. Androutsou,[i] M. Anguita,[j] L. Aphecetche,[k] M. Ardid,[l] S. Ardid,[l] H. Atmani,[m] J. Aublin,[n] L. Bailly-Salins,[o] Z. Bardačová,[q,p] B. Baret,[n] A. Bariego-Quintana,[c] S. Basegmez du Pree,[r] Y. Becherini,[n] M. Bendahman,[m,n] F. Benfenati,[t,s] M. Benhassi,[u,e] D. M. Benoit,[v] E. Berbee,[r] V. Bertin,[d] S. Biagi,[w] M. Boettcher,[x] D. Bonanno,[w] J. Boumaaza,[m] M. Bouta,[y] M. Bouwhuis,[r] C. Bozza,[z,e] R. M. Bozza,[f,e] H.Brânzaș,[aa] F. Bretaudeau,[k] R. Bruijn,[ab,r] J. Brunner,[d] R. Bruno,[a] E. Buis,[ac,r] R. Buompane,[u,e] J. Busto,[d] B. Caiffi,[ad] D. Calvo,[c] S. Campion,[g,ae] A. Capone,[g,ae] F. Carenini,[t,s] V. Carretero,[c] T. Cartraud,[n] P. Castaldi,[af,s] V. Cecchini,[c] S. Celli,[g,ae] L. Cerisy,[d] M. Chabab,[ag] M. Chadolias,[ah] A. Chen,[ai] S. Cherubini,[aj,w] T. Chiarusi,[s] M. Circella,[ak] R. Cocimano,[w] J. A. B. Coelho,[n] A. Coleiro,[n] R. Coniglione,[w] P. Coyle,[d] A. Creusot,[n] G. Cuttone,[w] R. Dallier,[k] Y. Darras,[ah] A. De Benedittis,[e] B. De Martino,[d] G. De Wasseige,[bd] V. Decoene,[k] R. Del Burgo,[e] I. Del Rosso,[t,s] U. M. Di Cerbo,[e] L. S. Di Mauro,[w] I. Di Palma,[g,ae] A. F. Díaz,[j] C. Diaz,[j] D. Diego-Tortosa,[w] C. Distefano,[w] A. Domi,[ah] C. Donzaud,[n] D. Dornic,[d] M. Dörr,[al] E. Drakopoulou,[i] D. Drouhin,[b,bc] R. Dvornický,[q] T. Eberl,[ah] E. Eckerová,[q,p] A. Eddymaoui,[m] T. van Eeden,[r] M. Eff,[n] D. van Eijk,[r] I. El Bojaddaini,[y] S. El Hedri,[n] A. Enzenhöfer,[d] G. Ferrara,[w] M. D. Filipović,[am] F. Filippini,[t,s] D. Franciotti,[w] L. A. Fusco,[z,e] J. Gabriel,[an] S. Gagliardini,[g] T. Gal,[ah] J. García Méndez,[l] A. Garcia Soto,[c] C. Gatius Oliver,[r] N. Geißelbrecht,[ah] H. Ghaddari,[y] L. Gialanella,[e,u] B. K. Gibson,[v] E. Giorgio,[w] I. Goos,[n] P. Goswami,[n] D. Goupilliere,[o] S. R. Gozzini,[c] R. Gracia,[ah] K. Graf,[ah] C. Guidi,[ao,ad] B. Guillon,[o] M. Gutiérrez,[ap] H. van Haren,[aq] A. Heijboer,[r] A. Hekalo,[al] L. Hennig,[ah] J. J. Hernández-Rey,[c] W. Idrissi Ibnsalih,[e] G. Illuminati,[t,s] M. de Jong,[ar,r] P. de Jong,[ab,r]

[*]Corresponding author.

https://doi.org/10.1088/1475-7516/2024/04/026

JCAP04(2024)026

B. J. Jung,[r] P. Kalaczyński,[as,be] O. Kalekin,[ah] U. F. Katz,[ah] A. Khatun,[q] G. Kistauri,[au,at] C. Kopper,[ah] A. Kouchner,[av,n] V. Kueviakoe,[r] V. Kulikovskiy,[ad] R. Kvatadze,[au] M. Labalme,[o] R. Lahmann,[ah] M. Lamoureux,[bd,*] G. Larosa,[w] C. Lastoria,[d] A. Lazo,[c] S. Le Stum,[d,*] G. Lehaut,[o] E. Leonora,[a] N. Lessing,[c] G. Levi,[t,s] M. Lindsey Clark,[n] F. Longhitano,[a] J. Majumdar,[r] L. Malerba,[ad] F. Mamedov,[p] J. Mańczak,[c] A. Manfreda,[e] M. Marconi,[ao,ad] A. Margiotta,[t,s,*] A. Marinelli,[e,f] C. Markou,[i] L. Martin,[k] J. A. Martínez-Mora,[l] F. Marzaioli,[u,e] M. Mastrodicasa,[ae,g] S. Mastroianni,[e] S. Miccichè,[w] G. Miele,[f,e] P. Migliozzi,[e] E. Migneco,[w] M. L. Mitsou,[e] C. M. Mollo,[e] L. Morales-Gallegos,[u,e] M. Morga,[ak] A. Moussa,[y] I. Mozun Mateo,[ax,aw] R. Muller,[r] M. R. Musone,[e,u] M. Musumeci,[w] S. Navas,[ap] A. Nayerhoda,[ak] C. A. Nicolau,[g] B. Nkosi,[ai] B. Ó Fearraigh,[ab,r] V. Oliviero,[f,e] A. Orlando,[w] E. Oukacha,[n] D. Paesani,[w] J. Palacios González,[c] G. Papalashvili,[at] V. Parisi,[ao,ad] E.J. Pastor Gomez,[c] A. M. Păun,[aa] G. E. Păvălaș,[aa] S. Peña Martínez,[n] M. Perrin-Terrin,[d] J. Perronnel,[o] V. Pestel,[ax] R. Pestes,[n] P. Piattelli,[w] C. Poirè,[z,e] V. Popa,[aa] T. Pradier,[b] J. Prado,[c] S. Pulvirenti,[w] G. Quéméner,[o] C.A. Quiroz-Rangel,[l] U. Rahaman,[c] N. Randazzo,[a] R. Randriatoamanana,[k] S. Razzaque,[ay] I. C. Rea,[e] D. Real,[c] G. Riccobene,[w] J. Robinson,[x] A. Romanov,[ao,ad] A. Šaina,[c] F. Salesa Greus,[c] D. F. E. Samtleben,[ar,r] A. Sánchez Losa,[c,ak] S. Sanfilippo,[w] M. Sanguineti,[ao,ad] C. Santonastaso,[az,e] D. Santonocito,[w] P. Sapienza,[w] J. Schnabel,[ah] J. Schumann,[ah] H. M. Schutte,[x] J. Seneca,[r] N. Sennan,[y] B. Setter,[ah] I. Sgura,[ak] R. Shanidze,[at] A. Sharma,[n] Y. Shitov,[p] F. Šimkovic,[q] A. Simonelli,[e] A. Sinopoulou,[a] M.V. Smirnov,[ah] B. Spisso,[e] M. Spurio,[t,s] D. Stavropoulos,[i] I. Štekl,[p] M. Taiuti,[ao,ad] Y. Tayalati,[m] H. Thiersen,[x] I. Tosta e Melo,[a,aj] E. Tragia,[i] B. Trocmé,[n] V. Tsourapis,[i] E. Tzamariudaki,[i] A. Vacheret,[o] A. Valer Melchor,[r] V. Valsecchi,[w] V. Van Elewyck,[av,n] G. Vannoye,[d,*] G. Vasileiadis,[ba] F. Vazquez de Sola,[r] C. Verilhac,[n] A. Veutro,[g,ae] S. Viola,[w] D. Vivolo,[u,e] J. Wilms,[bb] E. de Wolf,[ab,r] H. Yepes-Ramirez,[l] G. Zarpapis,[i] S. Zavatarelli,[ad] A. Zegarelli,[g,ae] D. Zito,[w] J. D. Zornoza,[c] J. Zúñiga[c] and N. Zywucka[x]

[a] *INFN, Sezione di Catania, Via Santa Sofia 64, Catania, 95123 Italy*

[b] *Université de Strasbourg, CNRS, IPHC UMR 7178, F-67000 Strasbourg, France*

[c] *IFIC — Instituto de Física Corpuscular (CSIC — Universitat de València), c/Catedrático José Beltrán, 2, 46980 Paterna, Valencia, Spain*

[d] *Aix Marseille Univ, CNRS/IN2P3, CPPM, Marseille, France*

[e] *INFN, Sezione di Napoli, Complesso Universitario di Monte S. Angelo, Via Cintia ed. G, Napoli, 80126 Italy*

[f] *Università di Napoli "Federico II", Dip. Scienze Fisiche "E. Pancini", Complesso Universitario di Monte S. Angelo, Via Cintia ed. G, Napoli, 80126 Italy*

[g] *INFN, Sezione di Roma, Piazzale Aldo Moro 2, Roma, 00185 Italy*

[h] *Universitat Politècnica de Catalunya, Laboratori d'Aplicacions Bioacústiques, Centre Tecnològic de Vilanova i la Geltrú, Avda. Rambla Exposició, s/n, Vilanova i la Geltrú, 08800 Spain*

[i] *NCSR Demokritos, Institute of Nuclear and Particle Physics, Ag. Paraskevi Attikis, Athens, 15310 Greece*

[j] *University of Granada, Dept. of Computer Architecture and Technology/CITIC, 18071 Granada, Spain*

JCAP04(2024)026

[k]Subatech, IMT Atlantique, IN2P3-CNRS, Nantes Université,
4 rue Alfred Kastler — La Chantrerie, Nantes, BP 20722 44307 France
[l]Universitat Politècnica de València, Instituto de Investigación para la Gestión Integrada de las Zonas Costeras, C/ Paranimf, 1, Gandia, 46730 Spain
[m]University Mohammed V in Rabat, Faculty of Sciences,
4 av. Ibn Battouta, B.P. 1014, R.P. 10000 Rabat, Morocco
[n]Université Paris Cité, CNRS, Astroparticule et Cosmologie, F-75013 Paris, France
[o]LPC CAEN, Normandie Univ, ENSICAEN, UNICAEN, CNRS/IN2P3,
6 boulevard Maréchal Juin, Caen, 14050 France
[p]Czech Technical University in Prague, Institute of Experimental and Applied Physics,
Husova 240/5, Prague, 110 00 Czech Republic
[q]Comenius University in Bratislava, Department of Nuclear Physics and Biophysics,
Mlynska dolina F1, Bratislava, 842 48 Slovak Republic
[r]Nikhef, National Institute for Subatomic Physics,
PO Box 41882, Amsterdam, 1009 DB Netherlands
[s]INFN, Sezione di Bologna, v.le C. Berti-Pichat, 6/2, Bologna, 40127 Italy
[t]Università di Bologna, Dipartimento di Fisica e Astronomia,
v.le C. Berti-Pichat, 6/2, Bologna, 40127 Italy
[u]Università degli Studi della Campania "Luigi Vanvitelli", Dipartimento di Matematica e Fisica,
viale Lincoln 5, Caserta, 81100 Italy
[v]E. A. Milne Centre for Astrophysics, University of Hull, Hull, HU6 7RX, United Kingdom
[w]INFN, Laboratori Nazionali del Sud, Via S. Sofia 62, Catania, 95123 Italy
[x]North-West University, Centre for Space Research,
Private Bag X6001, Potchefstroom, 2520 South Africa
[y]University Mohammed I, Faculty of Sciences,
BV Mohammed VI, B.P. 717, R.P. 60000 Oujda, Morocco
[z]Università di Salerno e INFN Gruppo Collegato di Salerno, Dipartimento di Fisica,
Via Giovanni Paolo II 132, Fisciano, 84084 Italy
[aa]ISS, Atomistilor 409, Măgurele, RO-077125 Romania
[ab]University of Amsterdam, Institute of Physics/IHEF,
PO Box 94216, Amsterdam, 1090 GE Netherlands
[ac]TNO, Technical Sciences,
PO Box 155, Delft, 2600 AD Netherlands
[ad]INFN, Sezione di Genova, Via Dodecaneso 33, Genova, 16146 Italy
[ae]Università La Sapienza, Dipartimento di Fisica, Piazzale Aldo Moro 2, Roma, 00185 Italy
[af]Università di Bologna, Dipartimento di Ingegneria dell'Energia Elettrica e dell'Informazione "Guglielmo Marconi", Via dell'Università 50, Cesena, 47521 Italia
[ag]Cadi Ayyad University, Physics Department, Faculty of Science Semlalia,
Av. My Abdellah, P.O.B. 2390, Marrakech, 40000 Morocco
[ah]Friedrich-Alexander-Universität Erlangen-Nürnberg (FAU), Erlangen Centre for Astroparticle Physics, Nikolaus-Fiebiger-Straße 2, 91058 Erlangen, Germany
[ai]University of the Witwatersrand, School of Physics,
Private Bag 3, Johannesburg, Wits 2050 South Africa
[aj]Università di Catania, Dipartimento di Fisica e Astronomia "Ettore Majorana",
Via Santa Sofia 64, Catania, 95123 Italy
[ak]INFN, Sezione di Bari, via Orabona, 4, Bari, 70125 Italy
[al]University Würzburg, Emil-Fischer-Straße 31, Würzburg, 97074 Germany

JCAP04(2024)026

[am]Western Sydney University, School of Computing, Engineering and Mathematics, Locked Bag 1797, Penrith, NSW 2751 Australia
[an]IN2P3, LPC, Campus des Cézeaux, 24 avenue des Landais BP 80026, Aubière Cedex, 63171 France
[ao]Università di Genova, Via Dodecaneso 33, Genova, 16146 Italy
[ap]University of Granada, Dpto. de Física Teórica y del Cosmos & C.A.F.P.E., 18071 Granada, Spain
[aq]NIOZ (Royal Netherlands Institute for Sea Research), PO Box 59, Den Burg, Texel, 1790 AB, the Netherlands
[ar]Leiden University, Leiden Institute of Physics, PO Box 9504, Leiden, 2300 RA Netherlands
[as]National Centre for Nuclear Research, 02-093 Warsaw, Poland
[at]Tbilisi State University, Department of Physics, 3, Chavchavadze Ave., Tbilisi, 0179 Georgia
[au]The University of Georgia, Institute of Physics, Kostava str. 77, Tbilisi, 0171 Georgia
[av]Institut Universitaire de France, 1 rue Descartes, Paris, 75005 France
[aw]IN2P3, 3, Rue Michel-Ange, Paris 16, 75794 France
[ax]LPC, Campus des Cézeaux 24, avenue des Landais BP 80026, Aubière Cedex, 63171 France
[ay]University of Johannesburg, Department Physics, PO Box 524, Auckland Park, 2006 South Africa
[az]Università degli Studi della Campania "Luigi Vanvitelli", CAPACITY, Laboratorio CIRCE — Dip. Di Matematica e Fisica — Viale Carlo III di Borbone 153, San Nicola La Strada, 81020 Italy
[ba]Laboratoire Univers et Particules de Montpellier, Place Eugène Bataillon — CC 72, Montpellier Cédex 05, 34095 France
[bb]Friedrich-Alexander-Universität Erlangen-Nürnberg (FAU), Remeis Sternwarte, Sternwartstraße 7, 96049 Bamberg, Germany
[bc]Université de Haute Alsace, rue des Frères Lumière, 68093 Mulhouse Cedex, France
[bd]UCLouvain, Centre for Cosmology, Particle Physics and Phenomenology, Chemin du Cyclotron, 2, Louvain-la-Neuve, 1349 Belgium
[be]AstroCeNT, Nicolaus Copernicus Astronomical Center, Polish Academy of Sciences, Rektorska 4, Warsaw, 00-614 Poland
E-mail: km3net-pc@km3net.de, mathieu.lamoureux@uclouvain.be, lestum@cppm.in2p3.fr, annarita.margiotta@unibo.it, vannoye@cppm.in2p3.fr

Abstract: The KM3NeT neutrino telescope is currently being deployed at two different sites in the Mediterranean Sea. First searches for astrophysical neutrinos have been performed using data taken with the partial detector configuration already in operation. The paper presents the results of two independent searches for neutrinos from compact binary mergers detected during the third observing run of the LIGO and Virgo gravitational wave interferometers. The first search looks for a global increase in the detector counting rates that could be associated with inverse beta decay events generated by MeV-scale electron anti-neutrinos. The second one focuses on upgoing track-like events mainly induced by muon (anti-)neutrinos in the GeV–TeV energy range. Both searches yield no significant excess for the sources in the gravitational wave catalogs. For each source, upper limits on the neutrino flux and on the total energy emitted in neutrinos in the respective energy ranges have been set. Stacking analyses of binary black hole mergers and neutron star-black hole mergers have also been performed to constrain the characteristic neutrino emission from these categories.

Keywords: neutrino astronomy, gravitational waves / sources, neutrino experiments

ArXiv ePrint: 2311.03804

JCAP04(2024)026

Contents

1 Introduction

The first detection of a gravitational wave (GW) signal from a binary compact merger [1] initiated in 2015 a new era in multi-messenger astronomy. The subsequent observation in 2017 of a GW signal from the binary neutron star merger event GW170817 and of prompt and afterglow electromagnetic emissions from the associated short gamma-ray burst [2] was the first and so far unique multi-messenger observation of its kind.

Models exist of production of neutrinos from these compact mergers, especially for mergers involving neutron stars such as binary neutron star mergers (BNS) [3] or neutron star-black hole mergers (NSBH) [4], though some models also predict neutrino emissions from binary black hole mergers (BBH) [5]. Although most of the studies focus on hadronic processes leading to high-energy neutrino production ($E_\nu \gtrsim$ GeV), thermal neutrinos in the MeV regime may also be produced [6].

Searches for neutrinos associated with GW signals from compact binary mergers have already been performed with other neutrino telescopes across the globe e.g., ANTARES [7, 8], IceCube [9–11], and Super-Kamiokande [12], without positive evidence of a common signal so far.

The KM3NeT detector, currently under construction, was taking data with a partial configuration during the third GW observation campaign in 2019-2020, allowing for a first search for neutrino counterparts. The article presents the dedicated analyses that have been developed for the search and the first results obtained with KM3NeT data, using the latest GW public catalogs as detailed below.

Two independent analyses have been performed, each of them optimized for the detection of a prompt signal in a short time window around the GW event, and for a specific neutrino

JCAP04(2024)026

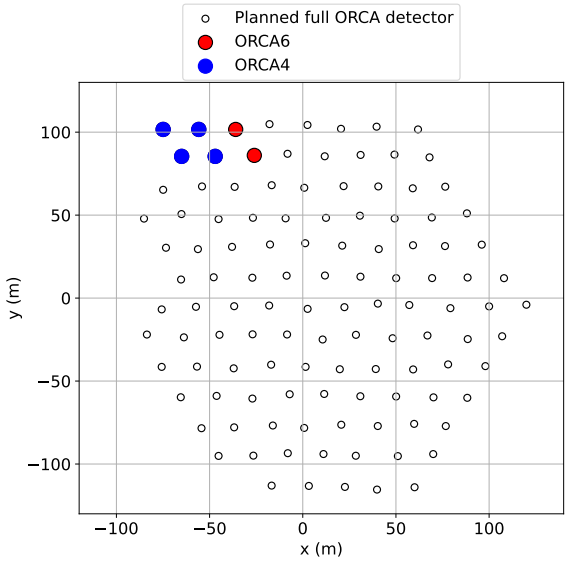

Figure 1. Footprint of the planned ORCA detector, with the ORCA4 and ORCA6 configurations highlighted in blue and red, respectively.

energy range. Section 2 describes the search for neutrinos in the 5–30 MeV range using a similar method to the one used to detect Core-Collapse Supernovae (CCSN) [13], while section 3 presents the search for neutrinos with energies from GeV to TeV.

The results of both searches are presented in section 4. The observations are converted into constraints on the incoming neutrino flux and on the total energy radiated in neutrinos for an isotropic emission around the source, in the relevant energy ranges, assuming a quasi-thermal distribution for MeV neutrinos and a single power law for GeV–TeV neutrinos. Additionally, for the latter, a stacked analysis has been performed to constrain the typical emission from BBH and NSBH objects. Results and prospects for future observations are discussed in section 5.

1.1 The KM3NeT neutrino telescope

The KM3NeT Collaboration is building two large-volume neutrino detectors in the depths of the Mediterranean Sea [14]. They rely on the detection of the Cherenkov light induced by charged particles produced in neutrino interactions, using about 200,000 three-inch photomultiplier tubes (PMTs). The PMTs are arranged in digital optical modules [15] (DOMs, with 31 PMTs each), deployed along vertical lines anchored at the sea bed, with 18 DOMs per line.

The KM3NeT/ORCA detector, located near Toulon (France), will be equipped with 115 such lines, with inter-line and inter-DOM spacings that are optimized for the detection of GeV-scale neutrinos and the study of atmospheric neutrino oscillations. The KM3NeT/ARCA detector is located near Capo Passero in Sicily (Italy) and will consist of two blocks of 115 lines, with larger spacings optimized for TeV–PeV astrophysical neutrinos.

Detection lines are currently being deployed on both sites. At the time of the GW observations in 2019–2020, ORCA was taking data with two lines (ORCA2) before July 1,

JCAP04(2024)026

2019, with four lines (ORCA4) during the period from July 1, 2019 to January 17, 2020, and then with six lines (ORCA6), as illustrated on the detector footprint in figure 1. The ORCA2 configuration is not considered in the following, as it is not large enough to perform a proper astrophysical search. The KM3NeT/ARCA detector has no data available for physics analysis during the considered period.

KM3NeT data is organized in consecutive runs of a few hours, and two main categories of neutrino events can be identified within the data. As it will be detailed in section 2, MeV neutrinos produce individually a very faint signal such that they can only be detected through a global increase of the detector counting rate linked to many MeV neutrinos interacting simultaneously. For higher energies (GeV and above), the total amount of deposited Cherenkov light distributed over multiple DOMs is sufficient to define unambiguously an event. This event would eventually be associated with an individual neutrino candidate.

1.2 The gravitational wave catalogs

The paper focuses on candidate binary mergers detected during the third observing run (O3) of the LIGO and Virgo GW interferometers reported in the three catalogs:

- GWTC-2 [16]: it reports 39 significant detections made during O3a, the first half of O3, running from April to September 2019.

- GWTC-2.1 [17]: this is an update of GWTC-2 with eight additional events detected during O3a but not reported in the previous catalog.

- GWTC-3 [18]: it reports 35 significant detections during O3b, the second half of O3, from November 2019 to March 2020. In addition, the catalog reports seven marginal candidates, out of which GW200105_162426 has been identified as an interesting NSBH candidate and is therefore included in the analysis, making the total number of selected events 36 for GWTC-3.

The data releases provided by the LIGO-Virgo Collaboration contain detailed information for each GW event including its timing $t_{\rm GW}$, the localization skymap $\mathcal{P}(\Omega)$, and the full posterior samples with all relevant source parameters: direction Ω, luminosity distance D_L, masses $m_{1,2}$, and total radiated energy in GWs $E_{\rm GW}$ (defined as the difference between the final object mass and the sum of the masses of the initial objects). The different categories of events (BBH, NSBH, BNS) are determined on the basis of the individual masses of the merging objects, with a chosen boundary at $m = 3\,{\rm M}_\odot$ separating between neutron stars (below) and black holes (above). Other parameters are used in the follow-up analyses detailed in the following sections.

The ORCA4 data-taking period overlaps with 19, 6, and 17 GW events in the GWTC-2, GWTC-2.1, and GWTC-3 catalogs, respectively, while ORCA6 overlaps with 19 GW events reported in the GWTC-3 catalog, for a total of 61 GW events. The remaining 20 (2) events in the GWTC-2 (GWTC-2.1) catalogs occurred before ORCA4 started.

JCAP04(2024)026

2 Search for neutrinos in the 5–30 MeV energy range

In a DOM, a hit is recorded when the voltage of a PMT rises above a 0.3 photoelectron threshold. Every hit is recorded and digitized before being grouped in segments of 100 ms called timeslices. Most of the recorded hits originate from optical noise due to radioactive decays in seawater, mainly ^{40}K (around 7 kHz per PMT), bioluminescence which can cause localized increases up to the MHz range, and atmospheric muons, as characterized in [19, 20].

In the 5–30 MeV energy range, KM3NeT is mainly sensitive to the inverse beta decay channel, where electron anti-neutrinos interact with free protons in the water to produce low-energy positrons. Those secondary particles emit Cherenkov light for only a few tens of centimeters. As the distance between optical modules is optimized for the detection of higher energy neutrinos (above few GeV), one such neutrino would only produce hits in a single DOM. Optical noise would also produce such a localized signal, making it indistinguishable from a single neutrino interaction.

Therefore, MeV neutrinos can only be detected as a global increase in the rate of coincidences between PMTs in single DOMs. The current method implemented to detect MeV neutrinos with the KM3NeT detector is optimized for the detection of a Galactic or near-Galactic CCSN, as described in [13, 21]. The method assumes a quasi-thermal neutrino distribution and an emission duration of around 500 ms, similar to what is expected for CCSN.

To reduce the contamination from optical noise, the concept of coincidence is defined. A coincidence consists of at least four hits within one DOM and with PMTs within a 90-degree opening angle, with all the hits in a time window of 10 ns. The coincidence level is then defined as the number of coincidences over the whole detector in a sliding window of 5 timeslices (with a total duration of 500 ms) and is estimated every 100 ms. This parameter is expected to follow a Poisson distribution, characterized by a parameter $\bar{b}_c$ referred to as the "expected background" in the following.

The search focuses on prompt neutrino emission coincident with the GW event, with similar timing as expected for a CCSN [22]. Existing models for prompt MeV neutrino emission from binary mergers have most of the signal in tens of milliseconds after the merger [6, 23], though the signal may extend up to a few seconds. However, to determine the time window during which the temporal correlation search is performed, it is necessary to consider the time-of-flight difference ΔT_{flight} between gravitational waves and MeV neutrinos (assuming the former travel at the speed of light):

$$\Delta T_{\text{flight}} < D_{\text{max}} \left(\frac{1}{v_\nu} - \frac{1}{c} \right) = \frac{D_{\text{max}}}{c} \left(\sqrt{1 + \frac{m_\nu^2 c^4}{p_\nu^2 c^2}} - 1 \right) \approx \frac{1}{2} \frac{D_{\text{max}}}{c} \frac{m_\nu^2 c^4}{E_\nu^2}, \tag{2.1}$$

where D_{max} is the estimated distance of the farthest GW source, v_ν, m_ν, p_ν, and E_ν are respectively the speed, mass, momentum, and energy of the neutrino. Given the current constraints on the neutrino mass [24, 25] and the distances of GW events reported in considered catalogs, it is found that $\Delta T_{\text{flight}} < 2\,\text{s}$.

The search window should be as short as possible to keep the trial factor (number of times the coincidence level is computed) low. A fixed time window of 2 s after the GW event, covering solely the bulk of the expected prompt signal and the maximum expected time-of-flight difference, is thus considered in the following.

JCAP04(2024)026

The search consists of three steps: the selection of runs with sufficient quality, the characterization of the background, and the search for a time-correlated signal in the 2 s window.

2.1 Run selection

The characterization of the coincidence levels due to the expected background is needed to perform the analysis. For each GW event, all data from the run covering the GW time is used, in addition to the specific coincidence levels during the corresponding 2 s time window. For five of those GW events, data acquisition issues prevented data from being retrieved. In order to remove occasional anomalies such as sparking PMTs, which may result in multiple coincidences happening in a single DOM during 100 ms, a quality score is computed in association with every coincidence level. The quality score, as described in [21], checks the consistency between the number of coincidences and the number of DOMs detecting at least one coincidence. A low score would indicate that one or several DOMs are producing an anomalous number of coincidences, which is not compatible with the expected background or signal. One additional GW event was removed from the studied sample due to a low-quality score within the 2 s time window, taking the total number of disregarded GW events to six. The analysis described below focuses on the 55 remaining GW events.

2.2 Background characterization

In the sea bioluminescence may lead to a localized increase of the hit rates up to the MHz level, causing the need to veto PMT with rates above ~ 100 kHz with the embedded electronics of the DOMs [26]. This leads to a non-constant number of active PMTs over the whole detector, which also causes variation in the expected background. The typical timescale of those variations is a few hours. The relation between these quantities is shown in figure 2, where every dot is the computed expected background averaged for the whole detector, for a given range of fraction of active PMTs, as obtained from ~ 200 runs, uniformly distributed in the ORCA4 and ORCA6 data-taking periods. As expected, a smaller fraction of active PMTs leads to a smaller expected background.

For each run containing a GW event, the expected background is inferred from the observed fraction of active PMTs based on a linear fit as shown in figure 2. The agreement between this expectation and the observed rate has been found to be sufficient for most of the runs containing a GW event, except the six ones between December 19, 2019 and January 25, 2020. The disagreement is due to a network issue between the ORCA detector and the shore station. Instead of using the linear fit, the expected background is directly taken from data for the six runs in question. As the fraction of active PMTs is relatively stable in the runs of interest, this expected background estimation is adequate.

2.3 Statistical analysis

As there is no event-by-event direction reconstruction of neutrinos at the MeV scale, the analysis consists only of a time coincidence search. For every GW event the 20 coincidence levels in the $[t_{\mathrm{GW}}, t_{\mathrm{GW}} + 2\,\mathrm{s}]$ time window (every 100 ms in the search window) are retrieved, as shown on the left panel of figure 3, and the maximum coincidence level c_{max} is extracted. Pseudo-experiments are then generated using the expected background $\bar{b}_c$ inferred from

JCAP04(2024)026

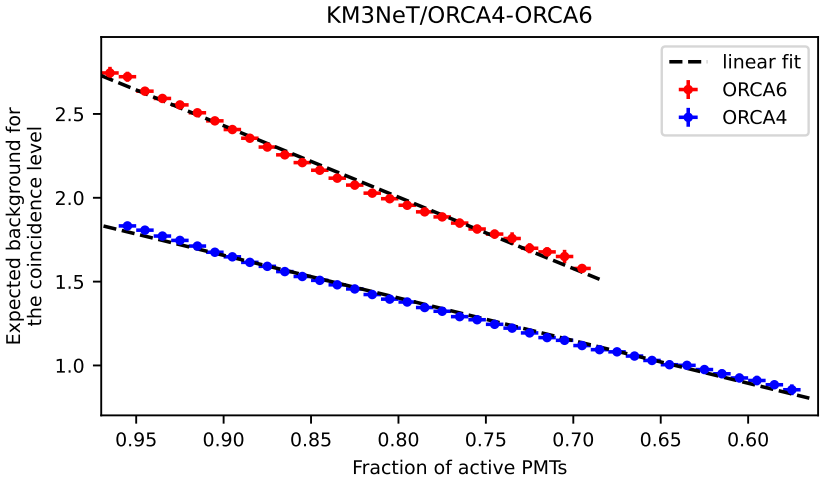

Figure 2. Expected background of the coincidence level as a function of the fraction of active PMTs for ORCA4 (blue) and ORCA6 (red). The crosses indicate averaged values over the full periods, and the dashed lines are linear fits to these points.

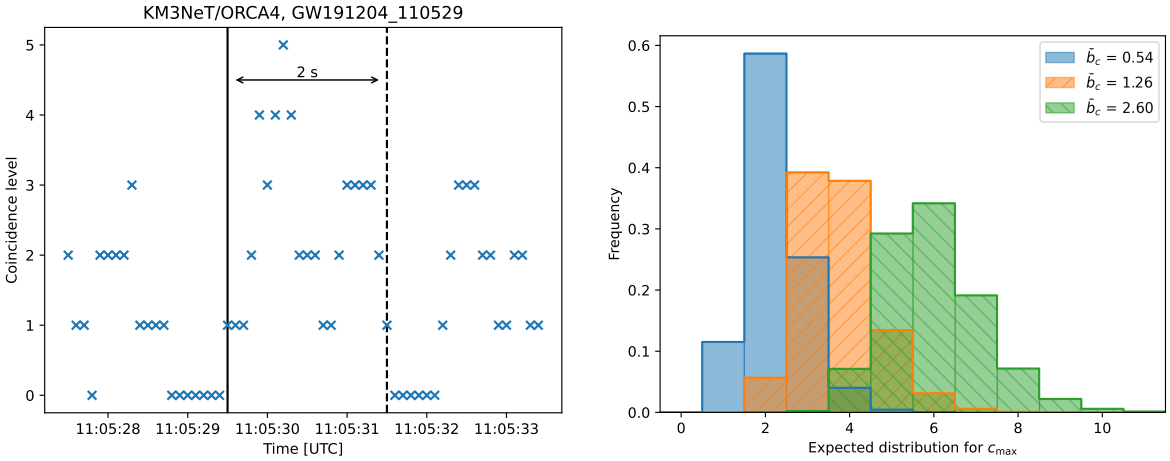

Figure 3. Timeline of the coincidence levels around GW101204_110529 (left) and distribution of the maximum coincidence level $c_{\max}$ for different values of the expected background $\bar{b}_c$ (right). On the left, the solid black line indicates the GW event time, and the dashed black line is the end of the 2 s time window during which the search is made.

the observed fraction of active PMTs (figure 4) averaged over the 2 s time interval. From those pseudo-experiments, the expected distributions of $c_{\max}$ are computed assuming only background and background + signal. Example distributions of $c_{\max}$ for different measured values of $\bar{b}_c$ are shown on the right panel of figure 3. Comparing these distributions with the observed $c_{\max}$ allows for the estimation of the corresponding p-value p and the 90% confidence level upper limit on the number of coincidences due to a neutrino signal $\mu_{\text{sig}}^{90\%}$ using the Feldman-Cousins [27] statistical approach.

In order to translate this quantity into physical limits, the number of expected signal events $\mu_{\text{sig,fulldet}}(E_0, D_{L,0})$ is computed for a reference CCSN at a distance $D_{L,0}$ with a neutrino fluence Φ_0 and a total released neutrino energy E_0, in a full ORCA detector

JCAP04(2024)026

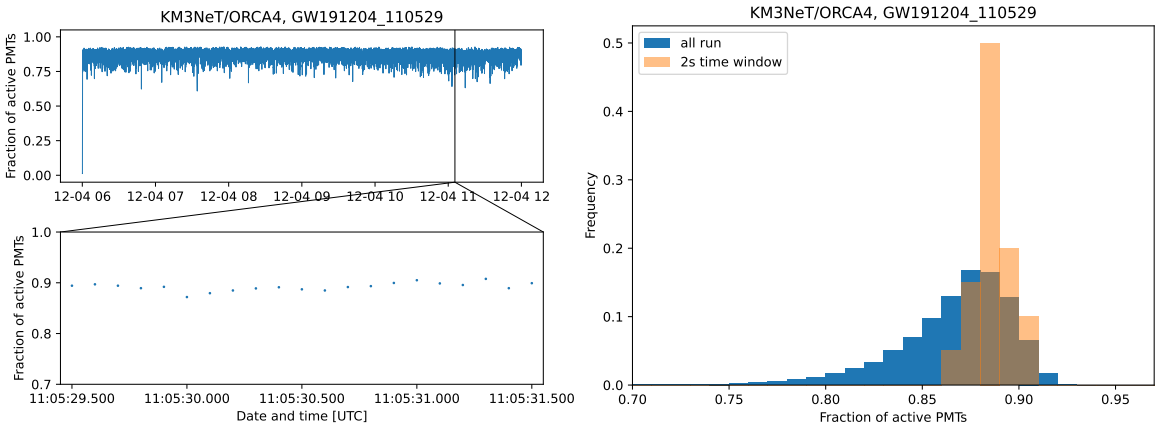

Figure 4. Time series (left) and distribution (right) of the fraction of active PMTs for the run covering GW191204_110529. On the left, the top plot shows the variability of the fraction of active PMTs during the run while the bottom plot is a zoom on the 2 s time window starting from the GW event time. On the right, the distribution of the fraction of active PMTs is shown in blue for every timeslice of the run and in orange for the 20 timeslices inside the 2 s time window.

(115×18 DOMs), and with perfect efficiency ($\eta = 1$, where η is the ratio of the measured expected background to the one when all PMTs are active). By correcting for the number of active DOMs $n_{\text{active DOMs}}$ and for η, an upper limit is obtained on the total neutrino fluence $\Phi^{90\%}$ and on the total energy emitted in MeV neutrinos by the source $E_{\text{tot},\nu}^{\text{iso},90\%}$:

$$\Phi^{90\%} = \frac{115 \times 18}{n_{\text{active DOMs}}} \times \frac{1}{\eta} \times \frac{\mu_{\text{sig}}^{90\%}}{\mu_{\text{sig,fulldet}}(E_0, D_{L,0})} \times \Phi_0 \tag{2.2}$$

$$E_{\text{tot},\nu}^{\text{iso},90\%} = \frac{115 \times 18}{n_{\text{active DOMs}}} \times \frac{1}{\eta} \times \frac{\mu_{\text{sig}}^{90\%}}{\mu_{\text{sig,fulldet}}(E_0, D_{L,0})} \times \frac{D_L^2}{D_{L,0}^2} \times E_0 \tag{2.3}$$

The reference values have been computed from refined simulations based on the work done in [13, 21], assuming a quasi-thermal emission of electron anti-neutrinos: $\mu_{\text{sig,fulldet}}(E_0, D_{L,0}) = 132.5$, $D_{L,0} = 10\,\text{kpc}$, $\Phi_0 = 8.2 \times 10^{10}\,\text{cm}^{-2}$, and $E_0 = 3 \times 10^{53}\,\text{erg}$.

3 Search for neutrinos in the GeV–TeV energy range

The search focuses on track-like events, mostly generated by muons produced in charged-current (CC) interactions of muon (anti-)neutrinos in the vicinity of the detector. Other event topologies are not investigated in this search.

The muon direction can be reconstructed by fitting the PMT hit patterns to the expected Cherenkov emission [28]. Only tracks reconstructed as upgoing or close to horizontal (i.e., with a reconstructed zenith direction θ such as $\cos(\theta) > -0.1$) are selected, in order to significantly reduce the bulk of background events caused by downgoing atmospheric muons. After this selection, the remaining backgrounds affecting the search for cosmic neutrinos are atmospheric neutrinos and atmospheric muons wrongly reconstructed as upgoing. At this level, the muon contribution is still dominant as it represents more than 99% of the observed event rate.

To further reduce the background, only events in time coincidence and in a direction compatible with the GW localization are considered. The time correlation is performed

JCAP04(2024)026

by selecting events in a time window $[t_{\rm GW} - 500\,{\rm s}, t_{\rm GW} + 500\,{\rm s}]$, a conservative estimate of the expected delay between the high-energy neutrino and the GW emission [29]. This time window is much larger than the one employed in section 2 as there is no problem with trial factor for the GeV–TeV search and it is therefore possible to probe not only prompt neutrino emission but also precursor or delayed processes. The source is assumed to be located within the region $\mathcal{R}_{90}$ containing 90% of the GW probability as built directly from the GW skymap $\mathcal{P}_{\rm GW}$. Then, the space correlation criterion corresponds to considering only events reconstructed with direction $\vec{x}$ within $\mathcal{R}_{90}^{+}$ defined as:

$$\mathcal{R}_{90}^{+} = \left\{ \vec{x} \,|\, \min_{\vec{d} \in \mathcal{R}_{90}} \left(\arccos\left(\vec{x} \cdot \vec{d}\right) \right) \leq \Delta\phi \right\}. \tag{3.1}$$

This extension aims to cover the detector's angular resolution and corresponds approximately to the 90% containment angle. In the following, $\Delta\phi$ is fixed to 30°; such a large value is due to the small size of ORCA4 and ORCA6 detectors which leads to a large tail in the angular error distribution, as illustrated in figure 7 in section 3.2. It should be significantly reduced with the expansion of the detector.

The analysis pipeline consists of three steps: a pre-selection of data to be analyzed according to its quality (section 3.1), an optimized event selection (section 3.2), and a statistical analysis to extract observation significance or upper limits on the neutrino emission (section 3.3).

3.1 Run selection

Careful checks have been implemented to ensure data quality and data-taking stability around each GW event. Conservative cuts are applied to remove all runs with non-stable trigger rates, or with other issues in terms of data quality, acquisition, or calibration. It reduces the considered total livetime (entire period of data taking, also beyond O3) from 181 to 174 days for ORCA4 and from 366 to 343 days for ORCA6.

It excludes nine GW candidates for which a follow-up is not possible as the corresponding detector runs are not selected. Furthermore, two additional GW events (GW200224_222234 and GW200311_115853) are excluded as they have been constrained by GW observations as being fully above the KM3NeT horizon. A total of 50 GW sources remain, including 44 BBHs and 6 NSBHs. The number differs from the one reported for MeV neutrinos in section 2, the chosen quality criteria being different as analyses rely on separate data streams with distinct responses to data-taking conditions.

The average rate of neutrino candidate events in the upgoing and horizontal region, in 2-day intervals, is shown in figure 5 for the two detector configurations superimposed on the time periods covered by the GW catalogs. The main cause of fluctuations in the rate of reconstructed events is the variability of the bioluminescence at the detector. This affects the number of active PMTs as discussed in section 2 which leads to fluctuations in the number of events and changes in the efficiency of track fitting.

3.2 Analysis pipeline

The number of events in the ON-zone region in the search time window and in the direction of the GW event is compared to the expected background from mis-reconstructed atmospheric muons and atmospheric neutrinos, as estimated from OFF-zone data.

JCAP04(2024)026

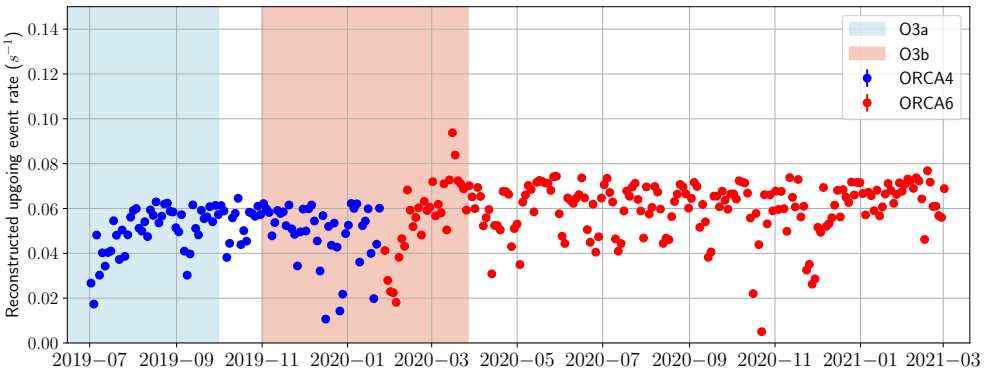

Figure 5. Rate of reconstructed upgoing events averaged over intervals of two days, for the two detector configurations ORCA4 (blue points) and ORCA6 (red points) in the data set. The shaded regions indicate the O3a and O3b periods.

A Boosted Decision Tree (BDT, based on gradient boosting [30]) model is applied to select signal-like events from the dominant atmospheric muon background [31]. It is trained with Monte Carlo simulations of ν_μ CC interactions (with neutrino energies up to 5 TeV) generated with gSeaGen [32] and muons simulated with MUPAGE [33]. The training uses a collection of 24 (14) features for ORCA4 (ORCA6), including low-level variables on the detected light as well as higher-level variables from track maximum likelihood fit results. The distribution of the final BDT scores is shown in figure 6 for data and for Monte Carlo simulations.

The ON-zone region refers to events within a ± 500 s time window centered on the GW event time, reconstructed as upgoing or horizontal tracks and in $\mathcal{R}_{90}^{+}$. The OFF-zone events are track-like events reconstructed within the same region in local coordinates, but at times incompatible with the GW. The OFF-zone background sample consists of a subset of runs during the same data period (ORCA4 or ORCA6) and with similar data-taking conditions with the run containing the GW event, as evaluated based on the event rate $R_{\rm loose}$ after a loose cut on the BDT score. Runs with rates in the range $[R^{\star}_{\rm loose} - \delta, R^{\star}_{\rm loose} + \delta]$ (where $R^{\star}_{\rm loose}$ is the event rate for the run containing the GW event) are selected, and the value of δ is optimized for each GW event to ensure $< 10\%$ statistical uncertainties while having a representative background estimate. The remaining data of the run containing the GW time, outside the ± 500 s time window, is also part of the background sample. The ratio between the livetimes of the ON-zone and the OFF-zone regions is denoted $\alpha_{\rm ON/OFF}$.

A model rejection factor (MRF, [34]) minimization is used to optimize the cut on the BDT score, with the signal being defined as an all-flavor E^{-2} neutrino spectrum, and the background being estimated from the OFF-zone region scaled by $\alpha_{\rm ON/OFF}$. The final cut may vary for each GW event so that the final expected background in the ON region depends on the detector conditions at the time of each GW. The detector effective area and acceptance after all cuts are estimated with the same E^{-2} signal Monte Carlo simulations. The sky is divided into pixels using the HEALPix method [35] and the direction-dependent acceptance $A(\Omega)$ is obtained for all pixels within the region $\mathcal{R}_{90}$.

JCAP04(2024)026

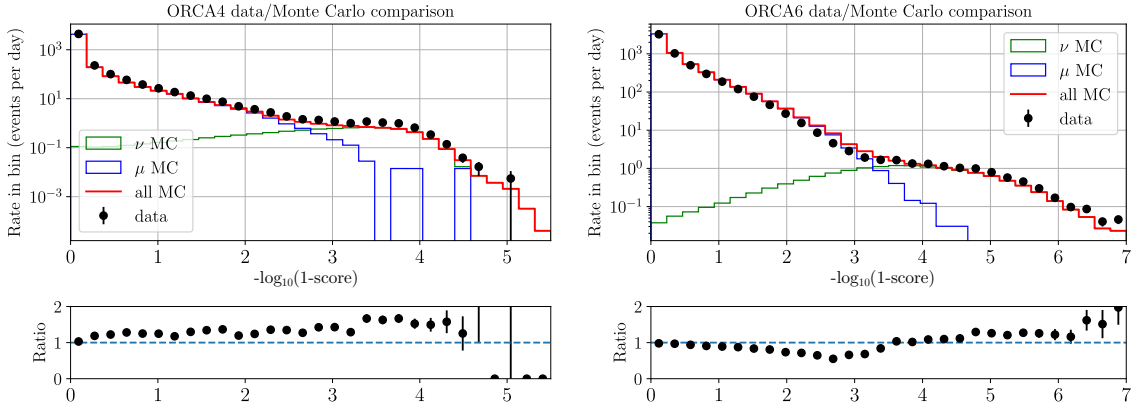

Figure 6. Comparisons of the score for upgoing events in data and Monte Carlo simulations, for the ORCA4 (left) and ORCA6 (right) detector configurations.

The average effective areas, event distributions, median angular resolution (defined as the 50% containment angle), and angular error are shown in figure 7 after score selection optimizations for a $\nu_\mu + \bar{\nu}_\mu$ flux of $10^{-4} E^{-2}$ GeV^{-1} cm^{-2} s^{-1}. It should be noted that in terms of angular resolution, ORCA4 seems to outperform ORCA6 at energies below 100 GeV as the optimized selection is stricter in this energy range for the 4-line configuration due to its smaller size so that only higher-quality events remain. It is reflected in the event distributions, as the rate of selected low-energy events is lower. When averaged over an E^{-2} spectrum, the median angular resolution for ORCA4 and ORCA6 are 1.85° and 1.63°, respectively. It corresponds roughly to containment angles in the energy region above 100 GeV on the bottom left plot of figure 7, as the events at these energies are those contributing the most to the overall expected flux.

The numbers of ON-zone events N_{ON} and OFF-zone events N_{OFF}, are respectively the number of events in the ON-zone and OFF-zone regions with a BDT score above the optimized cut. The mean expected number of background events in the ON-zone region is then

$$\bar{b} = \alpha_{\mathrm{ON/OFF}} \times N_{\mathrm{OFF}}. \tag{3.2}$$

The corresponding Poisson p-value p, the Poisson probability of observing at least N_{ON} events with an expected background of $\bar{b}$ events (neglecting the related statistical uncertainty for this computation), can thus be estimated.

3.3 Upper limit computation

Limits on the incoming neutrino flux for individual GW events. The number of detected events after all cuts is compared to the background expectation from the OFF-zone region. In the absence of a significant excess, upper limits on the neutrino emission are extracted using the Bayesian framework JANG [36].

Upper limits on the flux normalization ϕ assuming an all-flavor time-integrated neutrino spectrum $\mathrm{d}N/\mathrm{d}E = \phi \cdot (E/\mathrm{GeV})^{-2}$ are obtained, under the assumption of equipartition at Earth between neutrino flavors ($\nu_e : \nu_\mu : \nu_\tau = 1 : 1 : 1$). The corresponding likelihood

JCAP04(2024)026

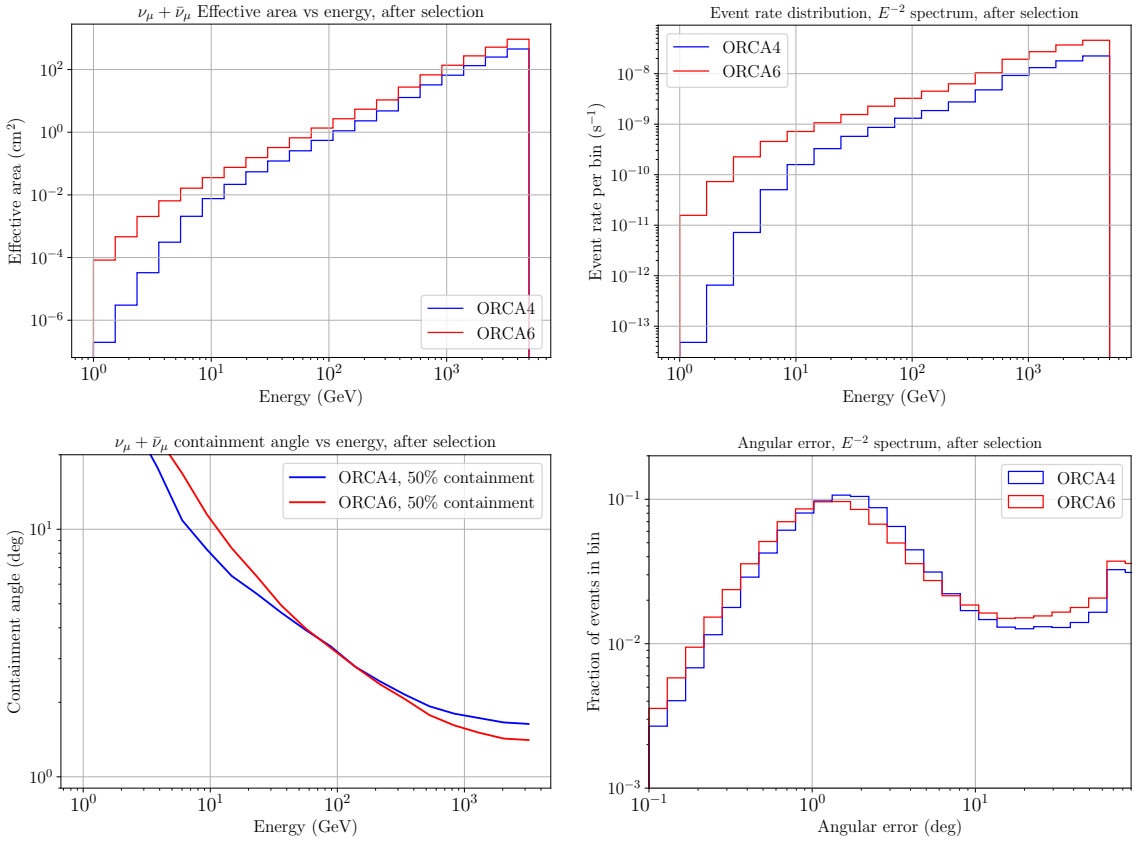

Figure 7. Performance of the $\nu_\mu + \bar{\nu}_\mu$ search, after optimized BDT score selection, in terms of effective area (top left), energy distribution (top right), median angular resolution (defined as the 50% containment angle, bottom left) and angular error (bottom right). These quantities are averaged over the set of runs used in the search and shown for the two detector configurations. The two plots on the right assume an incoming neutrino flux $10^{-4} E^{-2}$ GeV^{-1} cm^{-2} s^{-1}.

is defined as:

$$\mathcal{L}(N_{\rm ON}|b,\phi,A(\Omega)) = e^{-(b+A(\Omega)\cdot\phi)}\frac{(b+A(\Omega)\cdot\phi)^{N_{\rm ON}}}{N_{\rm ON}!}, \tag{3.3}$$

where b is the expected background and $A(\Omega) = a \cdot f(\Omega)$ is the direction-dependent detector acceptance, estimated with Monte Carlo simulations for each GW follow-up.

A Poisson prior $\pi(b)$ on the background with parameter $\lambda = b/\alpha_{\rm ON/OFF}$ encodes the information obtained from the measurements in the OFF-zone region. A 15% (10%) systematic uncertainty on the detector acceptance for ORCA4 (ORCA6) is reflected by defining a Gaussian prior on the acceptance normalization a. The GW localization skymap provided in the LIGO/Virgo catalogs is employed as prior knowledge on the source direction Ω: $\pi(\Omega) = \mathcal{P}(\Omega)$. Finally, a flat prior is considered for the parameter of interest ϕ. The posterior is then marginalized over nuisance parameters:

$$P(\phi) = C \iiint_{\Omega\in\mathcal{R}_{90}^{\rm vis}} \mathcal{L}(N_{\rm ON}|b,\phi,A(\Omega)) \times \pi(b; N_{\rm OFF}, \alpha_{\rm ON/OFF})\, \pi(a)\, \pi(\Omega)\, \pi(\phi)\, {\rm d}b\, {\rm d}a\, {\rm d}\Omega \tag{3.4}$$

JCAP04(2024)026

where the integration is performed with Monte Carlo integration techniques and C is a normalization constant. The marginalization over the source direction is only performed over the intersection $\mathcal{R}_{90}^{\rm vis}$ between the region $\mathcal{R}_{90}$ containing 90% of the GW probability and the visible sky using the KM3NeT upgoing track sample. The 90% upper limit on the time-integrated flux normalization $\phi^{90\%}$ is obtained by solving $\int_0^{\phi^{90\%}} P(\phi)\mathrm{d}\phi = 0.90$.

Limits on the total energy for individual GW events. Similarly, upper limits on the total energy emitted in neutrinos $E_{\rm tot,\nu}^{\rm iso} = 4\pi D_L^2 \int_{E_{\rm min}}^{E_{\rm max}} E \times (\mathrm{d}N/\mathrm{d}E)\,\mathrm{d}E$, or on the ratio between the neutrino emission and GW emission $f_\nu^{\rm iso} = E_{\rm tot,\nu}^{\rm iso}/E_{\rm GW}$, assuming an E^{-2} spectrum and isotropic emission, are also derived. The procedure is similar to the ones described above with the luminosity distance D_L as an additional parameter (and the total radiated energy $E_{\rm GW}$ as well for limits on f_ν). The integration bounds are fixed to $E_{\rm min} = 1\,\mathrm{GeV}$ and $E_{\rm max} = 100\,\mathrm{PeV}$ though the obtained results may be easily scaled for different choices of bounds (e.g. $E_{\rm tot,\nu}^{\rm iso} \propto \log(E_{\rm max}/E_{\rm min})$ for an E^{-2} spectrum).

Population studies. A stacking analysis of all BBH events is also performed by combining the individual follow-up results and constraining the typical $E_{\rm tot,\nu}^{\rm iso}$ ($f_\nu^{\rm iso}$) from those objects, assuming they have the same total energy released in neutrinos (the same ratio between neutrino and GW emissions). To account for the current analysis being limited to neutrinos below the horizon (and not all-sky sensitive), stacking pseudo-experiments are performed which include each GW follow-up with a probability equal to the visibility of the corresponding $\mathcal{R}_{90}$ region. This quantity is defined as the ratio between the integrated GW probabilities in $\mathcal{R}_{90}^{\rm vis}$ and in $\mathcal{R}_{90}$:

$$V = \frac{\int_{\mathcal{R}_{90}^{\rm vis}} \mathcal{P}(\Omega)\mathrm{d}\Omega}{\int_{\mathcal{R}_{90}} \mathcal{P}(\Omega)\mathrm{d}\Omega}. \tag{3.5}$$

The quoted limit is the median value obtained from these pseudo-experiments. A similar population study is performed considering the 6 NSBH candidates in the catalogs.

4 Results

The final results for the two analyses described in section 2 and section 3 are presented in table 1 and table 2 respectively. No excess has been found in any of the samples and follow-ups. Therefore, only upper limits on the neutrino emission are computed and reported in the same table. For the GeV–TeV analysis, due to the low expected background rates, the computed p-values are always either 1 (if $N_{\rm ON} = 0$) or typically smaller than 0.5 (if $N_{\rm ON} > 0$); the values are then only provided in the latter case.

JCAP04(2024)026

GW name	Merger type	$\bar{b}_c$	$c_{\max}$	FAR d^{-1}	p	$\Phi^{90\%}$ cm^{-2}	$E_{\mathrm{tot},\nu}^{\mathrm{iso},90\%}$ erg
ORCA4 period							
GW190701_203306	BBH	1.44	4	5.04×10^4	0.70	3.6×10^{10}	5.6×10^{61}
GW190706_222641	BBH	1.63	3	1.94×10^5	0.99	1.7×10^{10}	1.2×10^{62}
GW190707_093326	BBH	1.75	5	2.84×10^4	0.49	4.5×10^{10}	9.8×10^{60}
GW190708_232457	BBH	1.76	5	2.90×10^4	0.50	4.5×10^{10}	1.3×10^{61}
GW190719_215514	BBH	1.70	3	2.10×10^5	1.00	1.6×10^{10}	9.1×10^{61}
GW190725_174728	BBH	0.84	4	9.24×10^3	0.19	9.4×10^{10}	3.8×10^{61}
GW190727_060333	BBH	0.94	4	1.34×10^4	0.27	8.4×10^{10}	3.3×10^{62}
GW190728_064510	BBH	1.26	3	1.16×10^5	0.94	2.2×10^{10}	6.0×10^{60}
GW190731_140936	BBH	1.66	4	7.54×10^4	0.84	3.1×10^{10}	1.2×10^{62}
GW190805_211137	BBH	1.55	7	9.64×10^2	0.02	8.6×10^{10}	8.9×10^{62}
GW190814	NSBH	1.66	4	7.54×10^4	0.84	3.1×10^{10}	6.6×10^{59}
GW190828_063405	BBH	1.67	4	7.67×10^4	0.84	3.1×10^{10}	5.1×10^{61}
GW190828_065509	BBH	1.68	3	2.05×10^5	1.00	1.6×10^{10}	1.5×10^{61}
GW190909_114149	BBH	1.23	1	6.11×10^5	1.00	2.0×10^{10}	1.0×10^{62}
GW190917_114630	NSBH	1.73	4	8.44×10^4	0.87	3.0×10^{10}	5.7×10^{60}
GW190924_021846	BBH	1.77	4	8.98×10^4	0.89	2.9×10^{10}	3.5×10^{60}
GW190925_232845	BBH	1.71	4	8.18×10^4	0.86	3.0×10^{10}	9.6×10^{60}
GW190926_050336	BBH	1.79	3	2.30×10^5	1.00	1.5×10^{10}	7.9×10^{61}
GW190929_012149	BBH	1.79	3	2.30×10^5	1.00	1.5×10^{10}	2.5×10^{61}
GW190930_133541	BBH	1.72	3	2.14×10^5	1.00	1.6×10^{10}	3.3×10^{60}
GW191103_012549	BBH	1.73	4	8.44×10^4	0.87	3.0×10^{10}	1.1×10^{61}
GW191105_143521	BBH	1.80	4	9.39×10^4	0.90	2.9×10^{10}	1.4×10^{61}
GW191109_010717	BBH	1.24	4	3.23×10^4	0.53	4.2×10^{10}	2.5×10^{61}
GW191113_071753	BBH	1.75	4	8.71×10^4	0.88	3.0×10^{10}	2.0×10^{61}
GW191126_115259	BBH	1.26	5	8.14×10^3	0.17	6.3×10^{10}	6.0×10^{61}
GW191127_050227	BBH	1.71	4	8.18×10^4	0.86	3.0×10^{10}	1.3×10^{62}
GW191129_134029	BBH	1.78	1	7.18×10^5	1.00	1.1×10^{10}	2.4×10^{60}
GW191204_110529	BBH	1.64	5	2.24×10^4	0.41	4.8×10^{10}	5.7×10^{61}
GW191204_171526	BBH	1.54	4	6.11×10^4	0.77	3.4×10^{10}	5.2×10^{60}
GW191215_223052	BBH	1.74	3	2.19×10^5	1.00	1.6×10^{10}	2.1×10^{61}
GW191219_163120	NSBH	0.96	2	2.16×10^5	1.00	2.8×10^{10}	3.1×10^{60}
GW191222_033537	BBH	0.97	2	2.19×10^5	1.00	2.8×10^{10}	9.2×10^{61}
GW191230_180458	BBH	1.05	5	3.88×10^3	0.09	1.0×10^{11}	6.8×10^{62}

JCAP04(2024)026

GW name	Merger type	$\bar{b}_c$	$c_{\max}$	FAR d^{-1}	p	$\Phi^{90\%}$ cm^{-2}	$E_{\mathrm{tot},\nu}^{\mathrm{iso},90\%}$ erg
GW200105_162426	NSBH	1.14	4	2.49×10^4	0.44	6.9×10^{10}	1.9×10^{60}
GW200112_155838	BBH	1.15	4	2.56×10^4	0.45	6.9×10^{10}	3.9×10^{61}
GW200115_042309	NSBH	1.15	3	9.49×10^4	0.90	4.5×10^{10}	1.4×10^{60}
ORCA6 period							
GW200128_022011	BBH	1.21	3	1.06×10^5	0.93	6.4×10^{10}	2.7×10^{62}
GW200129_065458	BBH	1.23	3	1.10×10^5	0.93	3.3×10^{10}	9.8×10^{60}
GW200202_154313	BBH	0.54	1	3.61×10^5	1.00	7.5×10^{10}	4.6×10^{60}
GW200208_130117	BBH	1.27	3	1.18×10^5	0.95	3.2×10^{10}	5.8×10^{61}
GW200208_222617	BBH	1.30	4	3.72×10^4	0.59	5.9×10^{10}	3.7×10^{62}
GW200209_085452	BBH	1.29	2	3.19×10^5	1.00	3.2×10^{10}	1.3×10^{62}
GW200210_092254	NSBH	1.25	2	3.07×10^5	1.00	3.3×10^{10}	1.1×10^{61}
GW200216_220804	BBH	2.39	2	5.96×10^5	1.00	1.5×10^{10}	8.1×10^{61}
GW200219_094415	BBH	1.86	4	1.02×10^5	0.92	4.2×10^{10}	1.8×10^{62}
GW200220_061928	BBH	2.43	4	1.97×10^5	0.99	1.7×10^{10}	2.2×10^{62}
GW200220_124850	BBH	2.58	5	1.03×10^5	0.92	3.0×10^{10}	1.8×10^{62}
GW200224_222234	BBH	2.17	5	5.99×10^4	0.76	3.6×10^{10}	3.8×10^{61}
GW200225_060421	BBH	2.18	6	2.07×10^4	0.38	5.4×10^{10}	2.6×10^{61}
GW200302_015811	BBH	2.57	3	4.10×10^5	1.00	1.6×10^{10}	1.3×10^{61}
GW200306_093714	BBH	2.45	6	3.35×10^4	0.55	4.8×10^{10}	7.8×10^{61}
GW200308_173609	BBH	2.56	3	4.07×10^5	1.00	1.4×10^{10}	1.5×10^{62}
GW200311_115853	BBH	2.39	4	1.89×10^5	0.99	1.7×10^{10}	8.5×10^{60}
GW200316_215756	BBH	2.53	5	9.75×10^4	0.91	3.1×10^{10}	1.4×10^{61}
GW200322_091133	BBH	2.60	6	4.24×10^4	0.63	4.5×10^{10}	2.2×10^{62}

Table 1. Summary of O3 follow-up results of the MeV analysis. For each GW event, the third and fourth columns give the expected background $\bar{b}_c$ and the maximum observed coincidence level $c_{\max}$ during the 2 s window after the GW event. The next two columns report the False Alarm Rate (FAR, number of times per day one expects to observe $c_{\max}$ coincidences originating only from background) and the p-value. The last two columns provide the obtained upper limits on the neutrino emission, in terms of the incoming fluence and the total energy emitted in neutrinos.

JCAP04(2024)026

GW name	Merger type	V %	$\bar{b}$	$N_{\rm ON}$	p	$\phi^{90\%}$ $\mathrm{GeV^{-1}\,cm^{-2}}$	$E^{\rm iso,90\%}_{\rm tot,\nu}$ erg	$f^{\rm iso,90\%}_{\nu}$
ORCA4 period								
GW190706_222641	BBH	72	0.050	0	-	2.2×10^2	2.5×10^{58}	2.6×10^3
GW190707_093326	BBH	71	0.055	0	-	1.5×10^2	5.0×10^{56}	3.3×10^2
GW190708_232457	BBH	53	0.110	0	-	2.9×10^2	7.2×10^{56}	3.1×10^2
GW190719_215514	BBH	45	0.064	0	-	2.1×10^2	2.1×10^{58}	4.7×10^3
GW190725_174728	BBH	46	0.059	0	-	1.7×10^2	1.2×10^{57}	1.1×10^3
GW190727_060333	BBH	83	0.045	0	-	1.1×10^2	6.0×10^{57}	1.1×10^3
GW190728_064510	BBH	77	0.050	0	-	1.6×10^2	5.5×10^{56}	3.3×10^2
GW190731_140936	BBH	78	0.057	0	-	1.0×10^2	8.1×10^{57}	1.6×10^3
GW190803_022701	BBH	49	0.102	0	-	5.4×10^2	3.2×10^{58}	6.8×10^3
GW190805_211137	BBH	73	0.070	0	-	1.4×10^2	4.5×10^{58}	7.0×10^3
GW190814	NSBH	100	0.038	0	-	1.3×10^2	3.0×10^{55}	6.8×10^1
GW190828_063405	BBH	62	0.057	1	0.06	2.9×10^2	5.7×10^{57}	1.1×10^3
GW190828_065509	BBH	77	0.067	0	-	1.0×10^2	1.3×10^{57}	5.8×10^2
GW190909_114149	BBH	53	0.076	0	-	1.9×10^2	2.7×10^{58}	5.0×10^3
GW190915_235702	BBH	90	0.061	0	-	3.7×10^2	5.0×10^{57}	1.1×10^3
GW190916_200658	BBH	56	0.075	0	-	1.5×10^2	4.0×10^{58}	6.6×10^3
GW190917_114630	NSBH	73	0.066	0	-	1.8×10^2	4.9×10^{56}	1.4×10^3
GW190924_021846	BBH	40	0.043	0	-	1.6×10^2	2.6×10^{56}	2.7×10^2
GW190925_232845	BBH	100	0.059	0	-	1.4×10^2	5.9×10^{56}	1.9×10^2
GW190926_050336	BBH	53	0.052	0	-	1.6×10^2	2.9×10^{58}	6.2×10^3
GW190929_012149	BBH	67	0.075	0	-	1.6×10^2	1.3×10^{58}	2.0×10^3
GW190930_133541	BBH	22	0.073	0	-	4.6×10^2	1.4×10^{57}	9.9×10^2
GW191103_012549	BBH	43	0.063	0	-	4.0×10^2	2.4×10^{57}	1.6×10^3
GW191105_143521	BBH	85	0.067	0	-	1.5×10^2	9.5×10^{56}	6.9×10^2
GW191109_010717	BBH	88	0.070	0	-	1.3×10^2	1.5×10^{57}	2.3×10^2
GW191113_071753	BBH	72	0.070	0	-	1.3×10^2	1.7×10^{57}	1.3×10^3
GW191127_050227	BBH	43	0.079	0	-	1.4×10^2	1.5×10^{58}	2.4×10^3
GW191129_134029	BBH	62	0.059	0	-	1.2×10^2	3.2×10^{56}	2.5×10^2
GW191204_110529	BBH	45	0.084	0	-	1.4×10^2	4.9×10^{57}	1.6×10^3
GW191204_171526	BBH	85	0.041	0	-	1.2×10^2	2.1×10^{56}	1.3×10^2
GW191215_223052	BBH	64	0.052	0	-	1.6×10^2	3.1×10^{57}	9.8×10^2
GW191219_163120	NSBH	70	0.065	0	-	1.7×10^2	3.6×10^{56}	2.4×10^3
GW191222_033537	BBH	75	0.054	0	-	1.1×10^2	6.2×10^{57}	1.1×10^3

JCAP04(2024)026

GW name	Merger type	V %	$\bar{b}$	$N_{\rm ON}$	p	$\phi^{90\%}$ GeV^{-1} cm^{-2}	$E^{\rm iso,90\%}_{{\rm tot},\nu}$ erg	$f^{\rm iso,90\%}_{\nu}$
GW191230_180458	BBH	59	0.054	0	-	1.1×10^2	1.2×10^{58}	1.9×10^3
GW200105_162426	NSBH	53	0.158	0	-	1.9×10^2	6.7×10^{55}	1.7×10^2
GW200112_155838	BBH	45	0.116	0	-	1.9×10^2	1.1×10^{57}	2.1×10^2
ORCA6 period								
GW200128_022011	BBH	60	0.255	0	-	6.8×10^1	4.8×10^{57}	8.7×10^2
GW200129_065458	BBH	9	0.175	0	-	7.5×10^1	3.0×10^{56}	5.7×10^1
GW200208_130117	BBH	100	0.127	0	-	5.3×10^1	1.3×10^{57}	2.6×10^2
GW200209_085452	BBH	43	0.358	0	-	1.2×10^2	8.6×10^{57}	1.9×10^3
GW200210_092254	NSBH	27	0.258	0	-	7.6×10^1	3.2×10^{56}	6.8×10^2
GW200219_094415	BBH	91	0.213	0	-	7.6×10^1	4.7×10^{57}	1.0×10^3
GW200220_061928	BBH	60	0.290	0	-	6.2×10^1	1.8×10^{58}	1.8×10^3
GW200220_124850	BBH	54	0.286	0	-	7.6×10^1	1.0×10^{58}	2.2×10^3
GW200302_015811	BBH	61	0.497	1	0.39	2.1×10^2	2.9×10^{57}	7.2×10^2
GW200306_093714	BBH	49	0.367	0	-	2.1×10^2	7.7×10^{57}	2.5×10^3
GW200308_173609	BBH	55	0.335	1	0.28	1.2×10^2	1.3×10^{59}	4.5×10^4
GW200316_215756	BBH	3	0.261	1	0.23	7.9×10^1	5.4×10^{56}	3.7×10^2
GW200322_091133	BBH	50	0.376	0	-	1.7×10^2	1.3×10^{59}	3.7×10^5

Table 2. Summary of O3 follow-up results with the high-energy analysis. The second and third columns indicate the most probable merger type given the masses in the catalog and the GW localization visibility V at ORCA at the time of the merger. The next three columns report the mean expected number of background events $\bar{b}$, the observed number of events in the ON-zone region $N_{\rm ON}$, and the corresponding Poisson p-value p (in case of non-zero observations), and the last three are the obtained upper limits on the neutrino emission, in terms of the incoming time-integrated flux, the total energy emitted in neutrinos, and the ratio between neutrino and GW emissions.

Individual limits for the 5–30 MeV energy range. Only four events have a p-value lower than 0.2, with a minimum of 0.02, which is fully compatible with the background expectation. For the considered 2 s time window, the upper limits on the neutrino fluence range between 10^{10} and $10^{11}\,{\rm cm}^{-2}$, and on the total energy emitted in neutrinos between 10^{60} and 10^{63} erg, as reported in figure 8. Given that these limits are not very constraining with respect to the total available energy budget in the merger ($\lesssim 10^{55}$–10^{56} erg), stacking limits have not been estimated for this energy range.

Individual limits for the GeV–TeV energy range. The obtained upper limits on the total all-flavor isotropic energy $E^{\rm iso}_{{\rm tot},\nu}$ and on the ratio between the energy radiated in neutrinos and in GWs $f^{\rm iso}_{\nu} = E^{\rm iso}_{{\rm tot},\nu}/E_{\rm GW}$, for each of the 44 BBH and the 6 NSBH events, are shown in figure 9.

JCAP04(2024)026

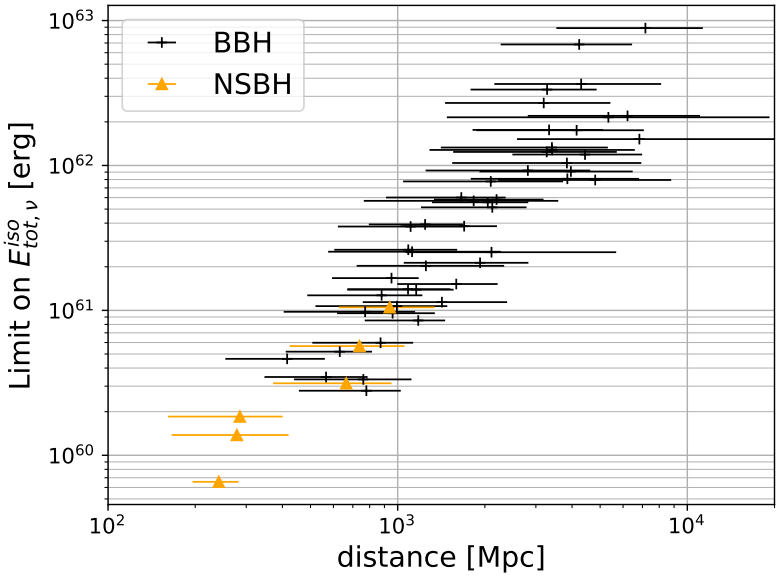

Figure 8. 90% upper limits on the total energy $E^{\rm iso}_{{\rm tot},\nu}$ emitted in neutrinos assuming a quasi-thermal distribution centered at 13 MeV, as a function of the source luminosity distance, assuming an E^{-2} spectrum and isotropic emission.

The most constraining individual limits for the BBH events are $E^{\rm iso,90\%}_{{\rm tot},\nu} = 2.1 \times 10^{56}$ erg (for GW191204_171526) and $f^{\rm iso,90\%}_{\nu} = 57$ (for GW200129_065458). Similarly, the most constraining individual NSBH event is the closest one, GW190814, with limits $E^{\rm iso,90\%}_{{\rm tot},\nu} = 3.0 \times 10^{55}$ erg and $f^{\rm iso,90\%}_{\nu} = 68$.

Limits from the stacking analysis in the GeV–TeV range. A stacking analysis is performed using the 44 BBH events followed up with KM3NeT. Assuming that all BBH emit the same typical total energy in neutrinos, a limit of $E^{\rm iso,90\%}_{{\rm tot},\nu} = 3.0 \times 10^{55}$ erg is obtained. Assuming instead that all sources have the same ratio between neutrino and GW emission, the limit is $f^{\rm iso,90\%}_{\nu} = 12$. The stacked total energy limit is seven times better than the most constraining individual event in this category.

The stacking of the six NSBH candidates followed with KM3NeT gives $E^{\rm iso,90\%}_{{\rm tot},\nu} = 1.9 \times 10^{55}$ erg and $f^{\rm iso,90\%}_{\nu} = 46$. Given the small number of NSBH events in the catalogs, the gain relative to the individual limits is moderate.

5 Discussion and conclusions

The limits presented in this paper cover two neutrino energy ranges: 5–30 MeV and GeV-TeV. Figure 10 illustrates the typical differential limits as a function of neutrino energy for ORCA4, ORCA6, and ANTARES [8], overlaid with the corresponding detector effective areas. For the two ORCA configurations, the bin at the highest neutrino energies is always the most constraining as the expected number of signal events in this bin is still relatively high (as shown in the top right panel of figure 7). The constraints derived here, with only a very partial ORCA detector (3-5% of the total number of lines to be deployed), already

JCAP04(2024)026

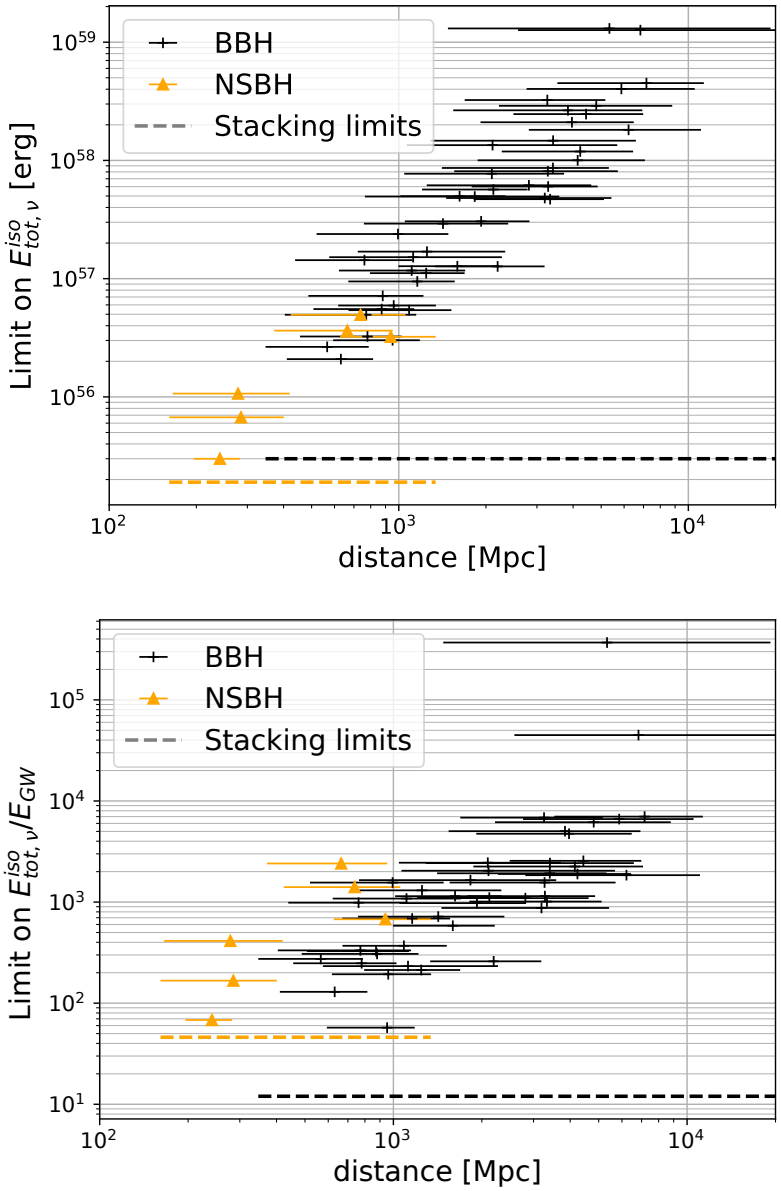

Figure 9. 90% upper limits on the total energy $E^{\rm iso}_{{\rm tot},\nu}$ emitted in neutrinos of all flavors (top) and on the ratio $f^{\rm iso}_{\nu} = E^{\rm iso}_{{\rm tot},\nu}/E_{\rm GW}$ (bottom) as a function of the source luminosity distance, assuming an E^{-2} spectrum and isotropic emission. The horizontal bars indicate the 5-95% range of the luminosity distance estimate, and the markers/colors correspond to the different source categories. The dashed bars correspond to the upper limits from the stacking analysis for BBH and NSBH categories.

JCAP04(2024)026

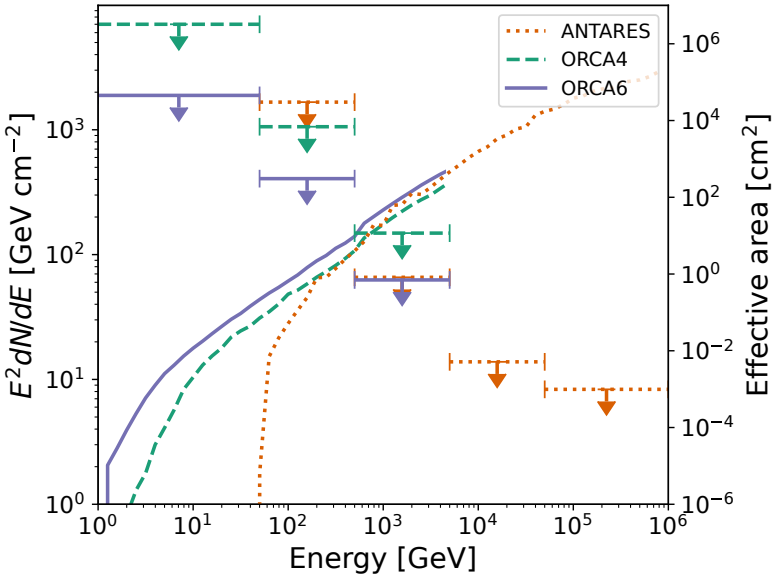

Figure 10. Comparison of ORCA effective areas at upgoing track selection level with ANTARES [8], for GW190814 (for ANTARES and ORCA4) and GW200208_130117 (for ORCA6). The two GW events have very similar sky coverage and thus comparable limits. The differential upper limits (horizontal lines) were obtained by considering independently bins in true neutrino energy and computing the corresponding limit on the flux normalization assuming an E^{-2} spectrum only within each bin (and zero elsewhere).

bring complementary information as the two ORCA configurations are sensitive in a lower energy range than ANTARES and they provide better differential limits in that region of the spectrum. The small size of the ORCA4 and ORCA6 configurations, combined with this difference in terms of energy range, lead to worse integrated limits when comparing to ANTARES or to IceCube high-energy limits [11], as illustrated on figure 11.

In the MeV range, the obtained limits are of the same order as the ones reported by KamLAND [37], although one to two orders of magnitude worse than Super-Kamiokande's [12], as shown on figure 11.

As of autumn 2023, 18 lines are operating for ORCA and 28 for ARCA, with more lines scheduled to be deployed later in 2023 and in the following years. During the following GW observation campaigns, especially O4 which has started in spring 2023, follow-ups will be performed with much larger detectors than discussed in this article, leading to improved sensitivities and an extended energy range coverage. More detailed neutrino emission models may also be explored, beyond the isotropic E^{-2} and quasi-thermal spectra investigated in the present study.

The ARCA configuration, which did not contribute to the present results for O3, is expected to participate for the first time in the follow-ups during O4. Its energy coverage at very high energy ($\gtrsim$ TeV) is complementary to ORCA, hence enhancing KM3NeT sensitivity and the discovery lever arm, especially for hard spectra. As the field of view of KM3NeT is very different from that of IceCube, even partial KM3NeT detectors will be able to contribute significantly to the searches, especially for sources localized in the Southern Sky.

JCAP04(2024)026

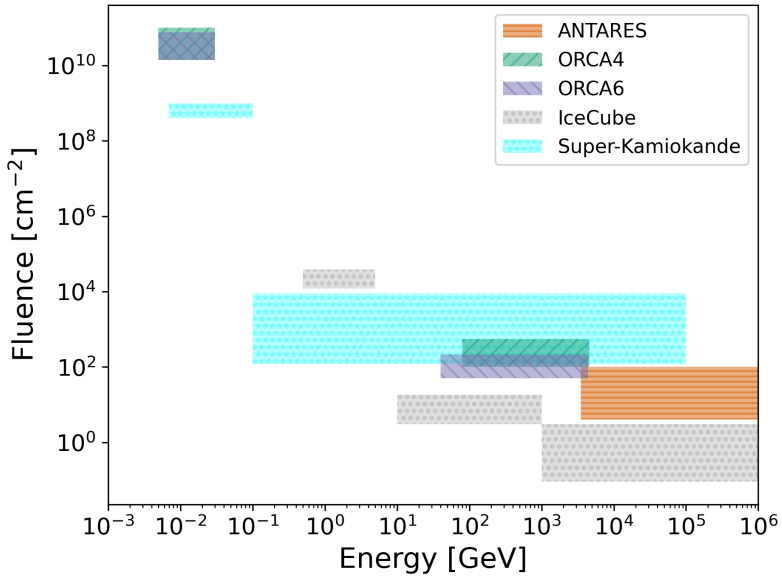

Figure 11. Range of 90% upper limits on the total neutrino fluence for both analyses. For MeV-scale neutrinos, these are directly the limits reported in table 1. For all reported results above 1 GeV, the fluence is computed integrating energies above 1 GeV ($\Phi = \int_{1\,\mathrm{GeV}} \phi E^{-2} \mathrm{d}E$), and the horizontal widths of the bands delimit the central energy range expected to contain 90% of the signal events (except for IceCube and Super-Kamiokande results where the full sensitive range is shown). The ANTARES limits are reported in [8]. The IceCube results are extracted from [10, 38], and [11], from left to right. The Super-Kamiokande results are obtained from [12, 39].

For MeV neutrinos, the gain is directly proportional to the size of the detector, as outlined in eq. (2.2), and KM3NeT is expected to reach similar sensitivities as Super-Kamiokande by the end of the construction.

The KM3NeT telescope is also performing real-time follow-ups during O4, planning to release results as fast as possible to help constrain the localization of a potential joint source and guide electromagnetic observations. It will improve the chance of identifying the corresponding electromagnetic emission and thus eventually constrain source models, jet structure, and production mechanisms.

Furthermore, the increasing number of detected GW sources, especially binaries involving neutron stars, will enhance the capability of stacking analyses. Even in the absence of individually significant sources, some hints of neutrino emission may arise for a sub-population of these sources, as a slight deviation from background-only predictions. Though the underlying production mechanisms are very different, covering different energy ranges from MeV to PeV with KM3NeT may help reveal the nature of the sources or identify sub-populations.

Acknowledgments

The authors acknowledge the financial support of the funding agencies: Agence Nationale de la Recherche (contract ANR-15-CE31-0020), Centre National de la Recherche Scientifique (CNRS), Commission Européenne (FEDER fund and Marie Curie Program), LabEx Uni-

JCAP04(2024)026

vEarthS (ANR-10-LABX-0023 and ANR-18-IDEX-0001), Paris Île-de-France Region, France; Shota Rustaveli National Science Foundation of Georgia (SRNSFG, FR-22-13708), Georgia; The General Secretariat of Research and Innovation (GSRI), Greece; Istituto Nazionale di Fisica Nucleare (INFN), Ministero dell'Università e della Ricerca (MIUR), PRIN 2017 program (Grant NAT-NET 2017W4HA7S) Italy; Ministry of Higher Education, Scientific Research and Innovation, Morocco, and the Arab Fund for Economic and Social Development, Kuwait; Nederlandse organisatie voor Wetenschappelijk Onderzoek (NWO), the Netherlands; The National Science Centre, Poland (2021/41/N/ST2/01177); The grant "AstroCeNT: Particle Astrophysics Science and Technology Centre", carried out within the International Research Agendas programme of the Foundation for Polish Science financed by the European Union under the European Regional Development Fund; National Authority for Scientific Research (ANCS), Romania; Grants PID2021-124591NB-C41, -C42, -C43 funded by MCIN/AEI/10.13039/501100011033 and, as appropriate, by "ERDF A way of making Europe", by the "European Union" or by the "European Union NextGenerationEU/PRTR", Programa de Planes Complementarios I+D+I (refs. ASFAE/2022/023, ASFAE/2022/014), Programa Prometeo (PROMETEO/2020/019) and GenT (refs. CIDEGENT/2018/034, /2019/043, /2020/049. /2021/23) of the Generalitat Valenciana, Junta de Andalucía (ref. SOMM17/6104/UGR, P18-FR-5057), EU: MSC program (ref. 101025085), Programa María Zambrano (Spanish Ministry of Universities, funded by the European Union, NextGenerationEU), Spain; The European Union's Horizon 2020 Research and Innovation Programme (ChETEC-INFRA — Project no. 101008324); Fonds de la Recherche Scientifique — FNRS, Belgium; Francqui foundation.

References

[1] LIGO Scientific and Virgo collaborations, *Observation of gravitational waves from a binary black hole merger*, *Phys. Rev. Lett.* **116** (2016) 061102 [arXiv:1602.03837] [INSPIRE].

[2] LIGO Scientific et al. collaborations, *Multi-messenger observations of a binary neutron star merger*, *Astrophys. J. Lett.* **848** (2017) L12 [arXiv:1710.05833] [INSPIRE].

[3] S.S. Kimura et al., *Transejecta high-energy neutrino emission from binary neutron star mergers*, *Phys. Rev. D* **98** (2018) 043020 [arXiv:1805.11613] [INSPIRE].

[4] S.S. Kimura, K. Murase, P. Mészáros and K. Kiuchi, *High-energy neutrino emission from short gamma-ray bursts: prospects for coincident detection with gravitational waves*, *Astrophys. J. Lett.* **848** (2017) L4 [arXiv:1708.07075] [INSPIRE].

[5] K. Kotera and J. Silk, *Ultrahigh energy cosmic rays and black hole mergers*, *Astrophys. J. Lett.* **823** (2016) L29 [arXiv:1602.06961] [INSPIRE].

[6] K. Kyutoku and K. Kashiyama, *Detectability of thermal neutrinos from binary-neutron-star mergers and implication to neutrino physics*, *Phys. Rev. D* **97** (2018) 103001 [arXiv:1710.05922] [INSPIRE].

[7] ANTARES collaboration, *Search for neutrino counterparts of gravitational-wave events detected by LIGO and Virgo during run O2 with the ANTARES telescope*, *Eur. Phys. J. C* **80** (2020) 487 [arXiv:2003.04022] [INSPIRE].

[8] ANTARES collaboration, *Search for neutrino counterparts to the gravitational wave sources from LIGO/Virgo O3 run with the ANTARES detector*, *JCAP* **04** (2023) 004 [arXiv:2302.07723] [INSPIRE].

JCAP04(2024)026

[9] IceCube collaboration, *IceCube search for neutrinos coincident with compact binary mergers from LIGO-Virgo's first gravitational-wave transient catalog*, *Astrophys. J. Lett.* **898** (2020) L10 [arXiv:2004.02910] [INSPIRE].

[10] IceCube collaboration, *Probing neutrino emission at GeV energies from compact binary mergers with the IceCube neutrino observatory*, arXiv:2105.13160 [INSPIRE].

[11] IceCube collaboration, *IceCube search for neutrinos coincident with gravitational wave events from LIGO/Virgo run O3*, *Astrophys. J.* **944** (2023) 80 [arXiv:2208.09532] [INSPIRE].

[12] Super-Kamiokande collaboration, *Search for neutrinos in coincidence with gravitational wave events from the LIGO-Virgo O3a observing run with the Super-Kamiokande detector*, *Astrophys. J.* **918** (2021) 78 [arXiv:2104.09196] [INSPIRE].

[13] KM3NeT collaboration, *The KM3NeT potential for the next core-collapse supernova observation with neutrinos*, *Eur. Phys. J. C* **81** (2021) 445 [arXiv:2102.05977] [INSPIRE].

[14] KM3Net collaboration, *Letter of intent for KM3NeT* 2.0, *J. Phys. G* **43** (2016) 084001 [arXiv:1601.07459] [INSPIRE].

[15] KM3NeT collaboration, *The KM3NeT multi-PMT optical module*, 2022 *JINST* **17** P07038 [arXiv:2203.10048] [INSPIRE].

[16] LIGO Scientific and Virgo collaborations, *GWTC-2: compact binary coalescences observed by LIGO and Virgo during the first half of the third observing run*, *Phys. Rev. X* **11** (2021) 021053 [arXiv:2010.14527] [INSPIRE].

[17] LIGO Scientific and VIRGO collaborations, *GWTC-2.1: deep extended catalog of compact binary coalescences observed by LIGO and Virgo during the first half of the third observing run*, *Phys. Rev. D* **109** (2024) 022001 [arXiv:2108.01045] [INSPIRE].

[18] KAGRA et al. collaborations, *GWTC-3: compact binary coalescences observed by LIGO and Virgo during the second part of the third observing run*, *Phys. Rev. X* **13** (2023) 041039 [arXiv:2111.03606] [INSPIRE].

[19] KM3NeT collaboration, *Deep sea tests of a prototype of the KM3NeT digital optical module*, *Eur. Phys. J. C* **74** (2014) 3056 [arXiv:1405.0839] [INSPIRE].

[20] KM3NeT collaboration, *The prototype detection unit of the KM3NeT detector*, *Eur. Phys. J. C* **76** (2016) 54 [arXiv:1510.01561] [INSPIRE].

[21] KM3NeT collaboration, *Implementation and first results of the KM3NeT real-time core-collapse supernova neutrino search*, *Eur. Phys. J. C* **82** (2022) 317 [arXiv:2109.05890] [INSPIRE].

[22] R.S.L. Hansen, M. Lindner and O. Scholer, *Timing the neutrino signal of a galactic supernova*, *Phys. Rev. D* **101** (2020) 123018 [arXiv:1904.11461] [INSPIRE].

[23] Y. Sekiguchi, K. Kiuchi, K. Kyutoku and M. Shibata, *Gravitational waves and neutrino emission from the merger of binary neutron stars*, *Phys. Rev. Lett.* **107** (2011) 051102 [arXiv:1105.2125] [INSPIRE].

[24] N. Palanque-Delabrouille et al., *Neutrino masses and cosmology with Lyman-α forest power spectrum*, *JCAP* **11** (2015) 011 [arXiv:1506.05976] [INSPIRE].

[25] F. Capozzi et al., *Unfinished fabric of the three neutrino paradigm*, *Phys. Rev. D* **104** (2021) 083031 [arXiv:2107.00532] [INSPIRE].

[26] KM3NeT collaboration, *KM3NeT front-end and readout electronics system: hardware, firmware and software*, *J. Astron. Telesc. Instrum. Syst.* **5** (2019) 046001 [arXiv:1907.06453] [INSPIRE].

JCAP04(2024)026

[27] G.J. Feldman and R.D. Cousins, *A unified approach to the classical statistical analysis of small signals*, *Phys. Rev. D* **57** (1998) 3873 [physics/9711021] [INSPIRE].

[28] KM3NeT collaboration, *KM3NeT/ARCA event reconstruction algorithms*, *PoS* **ICRC2017** (2018) 950 [INSPIRE].

[29] B. Baret et al., *Bounding the time delay between high-energy neutrinos and gravitational-wave transients from gamma-ray bursts*, *Astropart. Phys.* **35** (2011) 1 [arXiv:1101.4669] [INSPIRE].

[30] T. Chen and C. Guestrin, *XGBoost: a scalable tree boosting system*, arXiv:1603.02754 [DOI:10.1145/2939672.2939785] [INSPIRE].

[31] KM3NeT collaboration, *Real-time multi-messenger analysis framework of KM3NeT*, *PoS* **ICRC2021** (2022) 941 [INSPIRE].

[32] KM3NeT collaboration, *gSeaGen: the KM3NeT GENIE-based code for neutrino telescopes*, *Comput. Phys. Commun.* **256** (2020) 107477 [arXiv:2003.14040] [INSPIRE].

[33] G. Carminati et al., *MUPAGE: a fast atmospheric MUon GEnerator for neutrino telescopes based on PArametric formulas*, arXiv:0907.5563 [INSPIRE].

[34] G.C. Hill and K. Rawlins, *Unbiased cut selection for optimal upper limits in neutrino detectors: the model rejection potential technique*, *Astropart. Phys.* **19** (2003) 393 [astro-ph/0209350] [INSPIRE].

[35] K.M. Górski et al., *HEALPix — a framework for high resolution discretization, and fast analysis of data distributed on the sphere*, *Astrophys. J.* **622** (2005) 759 [astro-ph/0409513] [INSPIRE].

[36] M. Lamoureux, *Joint analysis of neutrinos and gravitational waves*, https://github.com/mlamo/jang.

[37] KamLAND collaboration, *Search for low-energy electron antineutrinos in KamLAND associated with gravitational wave events*, *Astrophys. J.* **909** (2021) 116 [arXiv:2012.12053] [INSPIRE].

[38] IceCube collaboration, *Gravitational wave follow-up using low energy neutrinos in IceCube DeepCore*, *PoS* **ICRC2021** (2021) 939 [arXiv:2107.11285] [INSPIRE].

[39] Super-Kamiokande collaboration, *Search for neutrinos in coincidence with gravitational wave events from the LIGO-Virgo O3a observing run with the Super-Kamiokande detector — data release*, Zenodo (2021).

JCAP04(2024)026